Journal of Zhejiang University-SCIENCE B (Biomedicine & Biotechnology) 2024 25(1):65-82
www.jzus.zju.edu.cn; www.springer.com/journal/11585
E-mail: jzus_b@zju.edu.cn

Research Article

https://doi.org/10.1631/jzus.B23d0004

Bioceramic scaffolds with two-step internal/external modification of copper-containing polydopamine enhance antibacterial and alveolar bone regeneration capability

Xiaojian JIANG[1], Lihong LEI[1], Weilian SUN[1], Yingming WEI[1], Jiayin HAN[1], Shuaiqi ZHONG[1], Xianyan YANG[2], Zhongru GOU[2]✉, Lili CHEN[1]✉

[1]*Department of Oral Medicine, the Second Affiliated Hospital, Zhejiang University School of Medicine, Hangzhou 310009, China*
[2]*Bio-nanomaterials and Regenerative Medicine Research Division, Zhejiang–California International Nanosystem Institute, Zhejiang University, Hangzhou 310058, China*

Abstract: Magnesium-doped calcium silicate (CS) bioceramic scaffolds have unique advantages in mandibular defect repair; however, they lack antibacterial properties to cope with the complex oral microbiome. Herein, for the first time, the CS scaffold was functionally modified with a novel copper-containing polydopamine (PDA(Cu^{2+})) rapid deposition method, to construct internally modified (*P), externally modified (@PDA), and dually modified (*P@PDA) scaffolds. The morphology, degradation behavior, and mechanical properties of the obtained scaffolds were evaluated in vitro. The results showed that the CS*P@PDA had a unique micro-/nano-structural surface and appreciable mechanical resistance. During the prolonged immersion stage, the release of copper ions from the CS*P@PDA scaffolds was rapid in the early stage and exhibited long-term sustained release. The in vitro evaluation revealed that the release behavior of copper ions ascribed an excellent antibacterial effect to the CS*P@PDA, while the scaffolds retained good cytocompatibility with improved osteogenesis and angiogenesis effects. Finally, the PDA(Cu^{2+})-modified scaffolds showed effective early bone regeneration in a critical-size rabbit mandibular defect model. Overall, it was indicated that considerable antibacterial property along with the enhancement of alveolar bone regeneration can be imparted to the scaffold by the two-step PDA(Cu^{2+}) modification, and the convenience and wide applicability of this technique make it a promising strategy to avoid bacterial infections on implants.

Key words: Copper-containing polydopamine; Modification; Antibacterial property; Bone regeneration; Angiogenesis; Bioceramic scaffold

1 Introduction

Periodontitis is a chronic infectious disease caused by dental plaque microorganisms, mainly characterized by the persistent and irreversible loss of alveolar bone. Severe periodontitis is the leading cause of tooth loss in adults (Kassebaum et al., 2014). Nowadays, bone substitute materials such as Geistlich Bio-OssTM are commonly used clinical implants in guided bone regeneration (GBR) surgery to achieve alveolar bone regeneration. However, a series of problems can occur during operation, such as shaping difficulty (Lei et al., 2019), poor mechanical stability (Mertens et al., 2019; Lei et al., 2020b), and potential disease transmission (Kim et al., 2013). Therefore, the development of novel ideal materials for bone tissue engineering has gradually become the focus of alveolar bone regeneration research.

Bioceramic materials, such as calcium silicate (CS)-based ceramics, have excellent biocompatibility as well as physicochemical and biological properties (Dong et al., 2018; Lei et al., 2020a). Silicon and other active ions released from CS can enhance the proliferation and differentiation of osteoblasts (OBs) (de Almeida et al., 2018). In our previous study, porous bioceramic scaffolds were constructed via three-dimension

---

✉ Lili CHEN, chenlili_1030@zju.edu.cn
Zhongru GOU, zhrgou@zju.edu.cn
Lili CHEN, https://orcid.org/0000-0002-0620-8844
Zhongru GOU, https://orcid.org/0000-0001-6718-0585

Received Mar. 21, 2023; Revision accepted Apr. 28, 2023;
Crosschecked Dec. 21, 2023

(3D) digital light processing (DLP) technology using magnesium-doped CS as a substrate (Qin et al., 2022). The introduction of magnesium could slow down the excessive degradation rate of CS-based scaffolds, and the released magnesium ions could promote angiogenesis and osteogenesis (Liu A et al., 2016; Sun et al., 2016). Moreover, the DLP technology makes it possible to construct an integrated scaffold consistent with the morphology of the bone defect, and it can precisely control the pore size and scaffold morphology, leading to bone regeneration enhancement (Qin et al., 2022; Wei et al., 2022; Lu et al., 2023). During the process of GBR, surgical wound dehiscence and membrane exposure are the most common complications (de Azambuja Carvalho et al., 2019). Once the membrane is exposed, oral microorganisms can migrate and colonize exposed sites, thereby impairing the effect of bone regeneration and even causing serious infections (Ye et al., 2011). Therefore, endowing the 3D ceramic scaffold with antibacterial ability is expected to improve the efficacy of bone regeneration.

Copper ions (Cu^{2+}) are widely used in tissue engineering for antibacterial purpose due to their potent and durable antibacterial activity and low drug resistance (Wang et al., 2016; Xu et al., 2020; Yang et al., 2022). Compared with antibacterial metal ions such as gold and silver, copper ions are essential trace elements for the human body; they play a major role in various life activities and can be excreted from the body through metabolism (Wojcieszak et al., 2017; Yang et al., 2021). In this aspect, numerous studies have confirmed that low concentrations of copper ions possess osteogenic and angiogenic effects (Wu et al., 2013; Kong et al., 2014; Wang et al., 2019). However, the potential cellular toxicity of high doses of copper ions may limit its application. Hence, it is highly beneficial to utilize copper ion concentration-dependent functional switches to unify the antibacterial potential and biological performances of copper.

Inspired by the superb viscosity of mussels, polydopamine (PDA) has been popular in tissue engineering as an excellent platform for modification due to its strong adhesion properties, numerous surface binding sites, outstanding photothermal effect, and remarkable biocompatibility (Lee et al., 2007; Sun et al., 2021; Hou et al., 2022; Yang et al., 2022). PDA can be formed simply by the spontaneous polymerization of dopamine under alkaline aerobic conditions (Lee et al., 2007; Hu et al., 2020). Recently, a novel technology using hydrogen peroxide (H_2O_2) and copper ions as catalysts was shown to facilitate the rapid deposition of PDA, shortening the polymerization process from days to hours (Zhang et al., 2016). In addition, copper ions can be simultaneously chelated in the PDA coating during polymerization. It is advantageous to utilize the antibacterial and osteogenic properties of copper ions for the modification of substrate with copper-containing PDA (PDA(Cu^{2+})) (Fan et al., 2019; Zhu et al., 2021). However, the optimization of personalized bioceramic scaffolds with PDA(Cu^{2+}) has not been thoroughly investigated.

Based on the aforementioned requirements, herein, we aimed to develop a two-step PDA(Cu^{2+}) modification strategy to endow the bioceramic scaffolds with multifunctional performances. On the one hand, with the help of spherical polymethyl methacrylate (PMMA) micro-carriers (about 15 μm) for PDA(Cu^{2+}) modification, the copper ions were evenly distributed in the micropore wall inside the pore struts of macroporous scaffolds, which was denoted as internal modification (*P) (Fig. 1a). These encapsulated copper ions could be slowly released along with the biodegradation of the bioceramic struts, leading to the promotion of osteogenesis and long-term antibacterial effect. On the other hand, the modification via integration with the PDA(Cu^{2+}) layer in the macropore wall was called as external modification (@PDA) (Fig. 1b). That is, the macropore wall surface of the externally modified scaffolds could release an appreciable dosage of copper ions in the early stage, which could exert an antibacterial role. Ultimately, combining these two-step modification methods at the same time (*P@PDA), a gradient multi-functional bone defect repair scaffold with antibacterial, osteogenic, and angiogenic functions was fabricated by utilizing the concentration-dependent function transition properties of copper ions (Fig. 1c).

2 Materials and methods

2.1 Synthesis of bioceramic powders

The 6% (molar fraction) magnesium-doped CS (CS-Mg6) powders were synthesized through a wet-chemical coprecipitation procedure described previously (Xie et al., 2016). After drying, the CS-Mg6 powders were calcined at 850 ℃ for 90 min. Then,

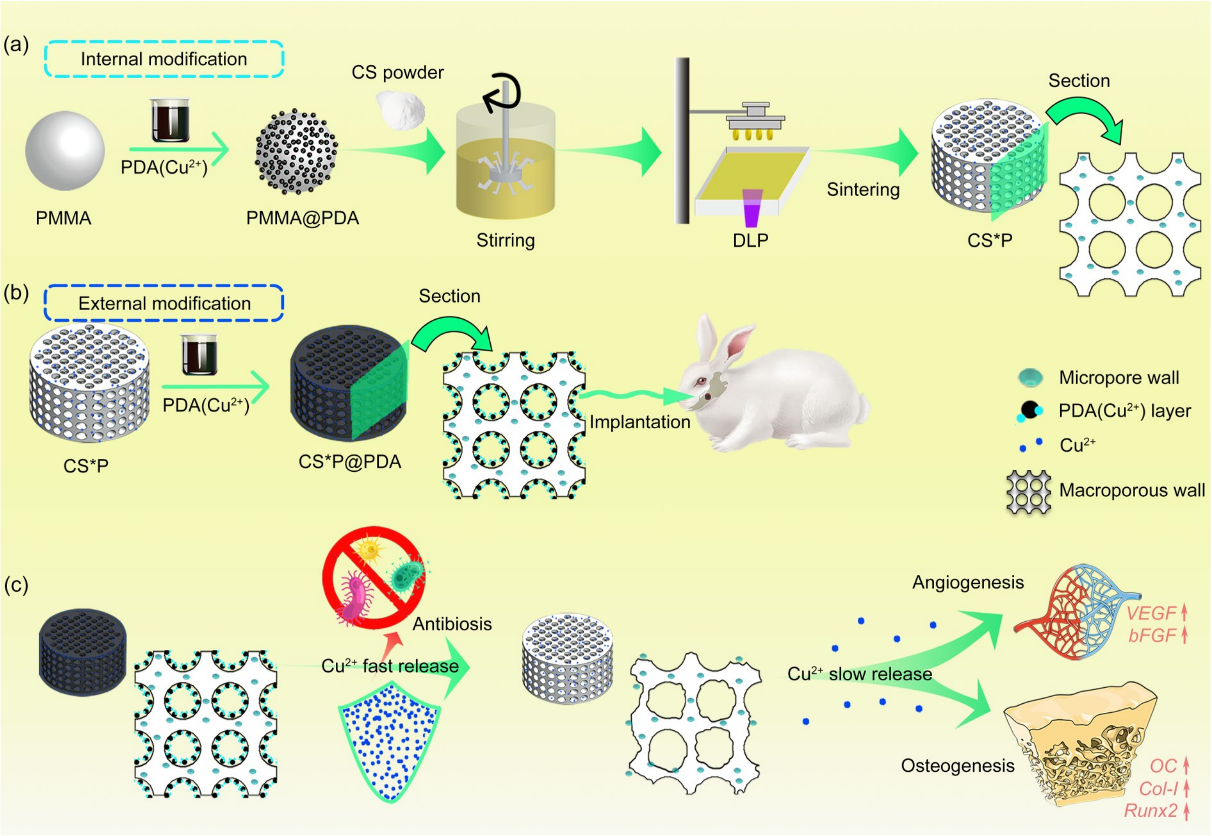

Fig. 1 Schematic illustration of the modification process and multifunctional mechanisms of two-step internal/external PDA(Cu^{2+})-modified bioceramic scaffolds. (a) The internal modification process of PDA(Cu^{2+}) on the scaffolds; (b) The external modification process of PDA(Cu^{2+}) on the scaffolds; (c) The pattern of two-step internal/external PDA(Cu^{2+})-modified bioceramic scaffolds gradually exerting antibacterial, osteogenic, and angiogenic effects after implantation. PDA(Cu^{2+}): copper-containing polydopamine; CS: calcium silicate; PMMA: polymethyl methacrylate; *P: internal modification; @PDA: external modification; *P@PDA: two-step internal/external modification; DLP: digital light processing; *VEGF*: vascular endothelial growth factor; *bFGF*: basic fibroblast growth factor; *OC*: osteocalcin; *Col-I*: type I collagen; *Runx2*: Runt-related transcription factor 2.

superfine CS-Mg6 powders (particle size$<$5 μm) were obtained by ball milling in alcohol for 6 h. The phase composition was verified by X-ray diffraction (XRD; Rigaku, Japan) analysis.

2.2 Preparation of calcium silicate scaffolds

The CS scaffolds were produced via a DLP 3D printer using photocurable resin (Ten Dimensions Technology Co., Beijing, China) as described previously (Lu et al., 2023). Briefly, a 3D model of cylindrical scaffolds with 600 μm circular pore channels was designed by SolidWorks 2019 software (Dassault Systems SolidWorks Corp., Waltham, MA, USA). The CS-Mg6 powders and resin were mixed at a mass ratio of 2:1 and stirred for 30 min to obtain a photocurable slurry. This was spread flat in the printer box and cured at every 200 μm by ultraviolet light. After washing and drying, the printed samples were sintered in a muffle furnace at 1150 °C for 120 min (the heating rate was 1.5 °C/min). The sintered bioceramic scaffolds with no modification were noted as CS group.

2.3 Preparation of CS*P@PDA scaffold

In order to introduce antibacterial properties, copper ions were selected for the external modification of CS through the rapid deposition technology of PDA coatings (Zhang et al., 2016). In simple terms, dopamine hydrochloride (2 mg/mL) was dissolved in Tris buffer solution (50 mmol/L, pH 8.5) with hydrogen chloride (HCl, 0.1 mol/L) to adjust the pH value. Then, copper sulfate pentahydrate ($CuSO_4 \cdot 5H_2O$, 5 mmol/L) and H_2O_2 (19.6 mmol/L) were added sequentially. Subsequently, CS scaffolds were put into the solution at the ratio of 3 g/50 mL and stirred continuously at room temperature for 1 h. Finally, the samples were washed twice with deionized water and dried at 60 °C for 4 h to complete the external modification of CS and noted as CS@PDA.

PMMA microspheres (about 15 μm at diameter) were coated with the same process to adsorb copper ions on the surface (noted as PMMA@PDA). The PMMA@PDA was used to replace 10% (mass fraction) CS powders in the photocurable slurry, which was called internal modification. Then, the CS*P group could be obtained with the follow-up procedure, similar to the CS group. The externally modified CS*P was noted as CS*P@PDA.

2.4 Analysis of morphology and surface structures

The surface structures and features of externally modified PMMA and each scaffold group were observed by scanning electron microscopy (SEM; G300, Zeiss, Germany). The presence of copper element was verified via energy-dispersive X-ray spectroscopy (EDS) at 15 kV accelerating voltage.

2.5 In vitro bio-dissolution and mechanical property analysis

The cylindrical scaffolds (5.2 mm (diameter)× 2.7 mm (thickness), n=12) were weighed (m_0) and soaked in Tris buffer (pH 7.4) at 37 °C with a solid/liquid ratio of 1.0 g/50 mL for six weeks. After immersion for 1, 3, 5, 7, 14, 28, and 42 d, 0.5 mL supernatant was extracted to detect the silicon (Si^{4+}), calcium (Ca^{2+}), magnesium (Mg^{2+}), and copper (Cu^{2+}) ions released by inductively coupled plasma (ICP; Thermo, USA), while equivalent fresh buffer was added into the soak medium. At every two weeks, the scaffolds (n=4) were extracted, washed with deionized water, and dried at 60 °C overnight before weighing (m_t). The mass loss rates were calculated according to the following formula: residual mass (%)=m_t/m_0×100%. Subsequently, the scaffolds were put on the universal testing machine (Instron 5566, Shanghai Zhuoji Testing Instruments Co., Ltd., Shanghai, China) to evaluate their compressive strength.

2.6 Hydrophilicity test

In order to facilitate the hydrophilicity test, four sets of solid discs (10.0 mm (diameter)×1.0 mm (thickness)) were fabricated using the same method as that for the scaffolds. The hydrophilicity was tested by an optical surface analyzer (OSA200-T, NBSI, Ningbo, China), and the droplet volume was set to 3 μL during the process.

2.7 In vitro antibacterial property

The antibacterial property of modified scaffolds was preliminarily tested with *Staphylococcus aureus* and *Escherichia coli*. *S. aureus* (ATCC 29213) and *E. coli* (ATCC 8099) were both kindly provided by Dr. Wangsiyuan TENG (The Second Affiliated Hospital, Zhejiang University, Hangzhou, China) and cultured in a Luria-Bertani (LB; Thermo, USA) agar slant medium at 37 °C. After sterilization, the scaffolds were placed in a 48-well plate, and then 200 μL bacterial suspension diluted to 1.0×10^6 colony-forming units (CFU)/mL was seeded onto the scaffolds. After incubation in a shaker at 37 °C for 40 min, 800 μL sterile saline was added into each well, followed by thorough blending with a pipette gun. Then, the bacterial suspension was inoculated on LB agar plates with ten-fold dilution series and incubated overnight at 37 °C. Finally, the bacterial viability rate was calculated based on the number of colonies on the plates using the following formula: bacterial viability rate (%)=$\text{CFU}_{\text{sample}}/\text{CFU}_{\text{blank}}$×100%.

2.8 Cell culture

Mouse primary OBs and human umbilical vein endothelial cells (HUVECs) were used in this study. The OBs were isolated from calvarial bones of 1-d old C57BL/6 mice as described previously (Doolittle et al., 2021). Briefly, the calvarial bones were cut into small pieces of 1–2 mm in length and washed in phosphate-buffered saline (PBS; Solarbio, Beijing, China). The pieces were cultured in complete Dulbecco's modified Eagle's medium (cDMEM) containing 10% (volume fraction) fetal bovine serum (FBS; Zhejiang Tianhang Biotechnology Co., Ltd., Huzhou, China) and 1% (volume fraction) penicillin-streptomycin (TBD, Tianjin, China) at 37 °C with 5% CO_2 in an incubator. After a large number of cells crawled out of the bone pieces, they were digested with 0.25% (volume fraction) trypsin-ethylenediaminetetraacetic acid (Genom, Hangzhou, China) and transferred to T75 cell culture dishes for expansion culture. OBs from three to five passages were used for the follow-up experiments. The HUVECs were kindly donated by Dr. Yuting YANG (Zhejiang University) and were also cultured in cDMEM.

2.9 Cell treatment

In order to simulate the real-time effects of scaffold extracts on cells as well as possible, scaffolds in each group were soaked in cDMEM at 0.1 g/mL (ISO 10993-12:2012 (International Organization for Standardization, 2012)) to obtain the extract during the same period of cell seeding (noted as cDMEM-extract). The next day, the cell culture media were replaced with the extract and refreshed every 2 d. Subsequently, fresh cDMEM was added to the extract plate for continued extraction (Fig. S1). The cells treated with unextracted media were set as the control group.

2.10 Cell viability assay

Cell viability was quantified with a cell counting kit-8 (CCK-8; Yeasen, Shanghai, China) according to the instructions of the manufacturer. Briefly, 100 μL of OBs were seeded onto 96-well plates at a density of 2.0×10^3 cells/well and incubated separately for 1, 3, and 7 d. After each culture time passed, OBs were gently rinsed twice with PBS after their medium was discarded. Then, an equal volume of mixture consisting of DMEM and CCK-8 solution (volume ratio=10:1) was added into each well in the dark. After incubation at 37 °C under a 5% carbon dioxide (CO_2) atmosphere for 1.5 h, the optical density (OD) was finally revealed at 450 nm with a spectrophotometer (Bio-Rad, CA, USA). The cell viability of HUVECs was tested in the same way, except that the incubation time was changed to 15 min.

2.11 qRT-PCR assay of osteogenesis- and angiogenesis-related genes

OBs were seeded onto 6-well plates at a density of 3.0×10^5 cells/well and incubated in 2 mL cDMEM-extract separately for 7 and 14 d. At each time point, the total RNAs of OBs were extracted via the RNAeasy™ Plus animal RNA isolation kit with spin column (Beyotime, Shanghai, China), and the reversed transcription of RNA was conducted using the Hifair® III 1st strand complementary DNA (cDNA) synthesis kit (EZBioscience, Beijing, China). The expression of target genes was performed with an SYBR green master mix kit (EZBioscience) on the ABI 7500 fast real-time polymerase chain reaction (PCR) system (Applied Biosystems, Foster City, CA, USA). The analysis of relative expression quantity was calculated using the comparative cycle threshold (CT) method ($\Delta\Delta C_T$). HUVECs were treated in the same way as OBs, while the incubation time was adjusted to 3 and 7 d. The detailed primer sequences were listed in Table 1.

2.12 Calcein-AM/PI double staining

The calcein-acetoxymethyl ester (AM)/propidium iodide (PI) double stain kit (Solarbio) was used to further evaluate the viability of cells cultured with cDMEM-extract. In brief, OBs were seeded onto 24-well plates at 1×10^4 cells/well and cultured with cDMEM-extract for 1 d. Afterwards, OBs were washed twice with PBS and treated with staining solution (1 mL 1× assay buffer with 2 μL calcein) at 37 °C in the dark for 25 min. Then, 5 μL PI was added into the solution for further staining at room temperature in the dark for 5 min. Finally, the stained cells were observed under a fluorescence microscope (Zeiss).

2.13 Alkaline phosphatase staining assay

OBs were seeded onto 24-well plates at a density of 1×10^4 cells/well. On the next day, culture media were replaced with extracts from scaffolds soaked in osteogenic media (noted as Ind-extract), which were based on cDMEM supplemented with 10 nm dexamethasone (Sigma, USA), 50 μg/mL L-ascorbic acid (Sigma), and 10 mmol/L β-glycerophosphate (Sigma). After 7 and

Table 1 Primer sequences used in this study

Gene	Forward (5'→3')	Reverse (5'→3')
mGAPDH	TGTGCCGTCGTGGATCTGA	TTGCTGTTGAAGTCGCAGGAG
Col-I	ATGCCGCGACCTCAAGATG	TGAGGCACAGACGGCTGAGTA
OC	AGCGCTTGGCCCAGACCTA	TAGCGCCGGAGTCTGTTCACTAC
Runx2	CTATCTGAGCCAGATGACATCCC	GTGGCAGTGTCATCATCTGAAATAC
hGAPDH	AGATCCCTCCAAAATCAAGTGG	GGCAGAGATGATGACCCTTTT
VEGF	TGCGGATCAAACCTCACCA	CAGGGATTTTTCTTGTCTTGCT
bFGF	GGAGAAGAGCGACCCTCACATCA	CATAGCCAGGTAACGGTTAGCACAC

mGAPDH: mouse glyceraldehyde-3-phosphate dehydrogenase (GAPDH); *Col-I*: type I collagen; *OC*: osteocalcin; *Runx2*: Runt-related transcription factor 2; *hGAPDH*: human GAPDH; *VEGF*: vascular endothelial growth factor; *bFGF*: basic fibroblast growth factor.

14 d of osteogenic induction, OBs were placed in a fixative solution (Fdbio, Hangzhou, China) for 30 min and stained using a 5-bromo-4-chloro-3-indolyl phosphate (BCIP)/nitro blue tetrazolium (NBT) alkaline phosphatase (ALP) color development kit (Beyotime).

2.14 Scratch wound assay

The cell migration ability was determined by the scratch wound assay. First, horizontal lines on the back of the 6-well plate were scribed with a marker to ensure the consistency of the observation points before and after the test. Then, HUEVCs were grown to full confluence with cDMEM in 6-well plates and wounded with sterile 1 mL pipette tips. Immediately afterwards, the detached cells from the plates were removed by washing twice with PBS, and the remaining cells were incubated with cDMEM-extract for 12 and 24 h. The progress of HUVEC migration into the wound was photographed using a light microscope (Leica, Germany). The wound healing rate was analyzed via ImageJ software (National Institutes of Health (NIH), Bethesda, USA) and calculated as (1−(current wound area)/(original wound area)×100%).

2.15 In vivo analysis of the efficacy of bone defect repair

Rabbit bilateral mandibular defect models were used to compare the osteogenic efficacy of CS and CS*P@PDA with the blank group. Nine male New Zealand white rabbits (2.8–3.2 kg) with a total of 18 defect sites were randomly divided into three groups. Each rabbit was fed in a single cage and acclimated for one week before surgery. General anesthesia was administered by ear vein injection of 3% (0.03 g/mL) pentobarbital sodium (1.0 mL/side; Merck, Germany), whereas 2% (0.02 g/mL) lidocaine (1.0 mL/side; Harbin Sanma Veterinary Drug Co., Harbin, China) was used for local anesthesia. Subsequently, cylindrical bone defects (8.0 mm (diameter)×4.0 mm (thickness)) were created on the mandibles with a high-speed drill under continuous saline cooling. The scaffolds prepared for the animal experiment were implanted into the defects, and the defects without implantation were set as the blank group.

Next, the incisions were sutured layer-by-layer with the topical application of penicillin, and after surgery, penicillin (30 000 U/kg) was injected intramuscularly once daily for 3 d to prevent infection. The rabbits were euthanized at four weeks, and the mandibular specimens with scaffolds were harvested and fixed in 4% (volume fraction) formalin (Biosharp, Beijing, China) for further analyses.

2.16 Microcomputed tomography examination

Six specimens in each group (blank, CS, and CS*P@PDA) were scanned via a high-resolution microcomputed tomography (μCT) system (Inveon, Siemens, Germany) to evaluate the osteogenic behavior in the defects. The region of interest (ROI; 8.0 mm (diameter)× 4.0 mm (thickness)) was selected manually along the defect edge and virtually 3D-reconstructed. The newly formed bone volume (BV)/total volume (TV) ratio, scaffold residual volume (RV)/TV ratio, and trabecular number (Tb.N) were calculated using Inveon Acquisition Workplace (IAW; Siemens) for quantitative analysis.

2.17 Histological analysis

Following μCT examination, the specimens were dehydrated in a series of ethanol (80%–100%, volume fraction) and embedded in polymethylmethacrylate. Afterwards, serial sections were cut in the defect sites (from lingual to buccal direction), and the sections with a thickness of 10 μm were stained with hematoxylin/eosin (HE) and tetrachrome stain (MacNeal). A light microscope (DMLA, Leica) was used to observe the stained sections under different magnification rates (15× and 40×). Histomorphometric analysis of the new bone and vessels was conducted using ImageJ software, and at least six randomly selected fields under high magnification of each group were applied for statistical analysis.

2.18 Statistical analysis

All data were analyzed using the statistical software SPSS 19.0 (IBM, Armonk, NY, USA), and the quantitative results were expressed as mean±standard deviation (SD). The differences among multiple groups were measured via one-way analysis of variance (ANOVA), and those between two groups were evaluated by Student's *t*-test. In all cases, $P<0.05$ was considered as statistically significant.

3 Results

3.1 Analysis of bioceramic powders

According to the XRD analysis, the crystalline phase of CS-Mg6 powder was consistent with the diffraction peaks of β-phase wollastonite in power diffraction file (PDF#76-0925; Fig. 2a). To confirm the Mg doping proportion in the CS-Mg6 powder, ICP analysis showed that the Mg-substituting-Ca molar fraction was 6.73% (Table S1), and the Mg content in the CS-Mg6 powder was 1.40% in mass.

3.2 Characterization of modified scaffolds

As mentioned in Figs. 1a and 1b, the fabricating process for the multifunctional scaffolds included two-step internal and external modifications. As for the internal modification (CS*P) scaffolds, the PMMA microspheres (about 15 μm) were used as micro-carriers of copper ions into scaffolds. It was evident that the PMMA microspheres could be adhered by the PDA(Cu^{2+}) via both SEM observation and line-scanning energy-dispersive X-ray (EDX) analysis (Figs. 2b–2e). Meanwhile, based on the gross appearances, all scaffolds with or without modification were consistent with the designed macroporous architectures (Fig. 2f). As expected, it was observed that the bioceramic slurry free of PMMA microspheres would produce a denser macropore wall in the bioceramic scaffolds (CS scaffolds), in comparison with the 3D-printed constructs with PMMA microspheres (CS*P and CS*P@PDA). It was reasonable to assume that after high-temperature sintering treatment, the PMMA microspheres with PDA were volatilized, leaving a great amount of copper ions in the micropore wall of scaffolds. In contrast, the external modification did not involve a high-temperature process, so a great number of PDA nanoparticles could be seen on the surface of CS@PDA scaffolds. For instance, the PMMA-derived micropores and a tremendous amount of PDA nanoparticles were found on the surface of CS*P@PDA scaffolds (Figs. 2g and 2h).

3.3 Mechanical, bio-dissolution, and hydrophilic properties of scaffolds

In order to clarify the bio-dissolution behavior of the fabricated scaffolds, especially to further explore the release pattern of copper ions, the scaffolds were immersed in Tris buffer for up to six weeks. ICP analysis revealed the changes in the released ion concentration during immersion (Figs. 3a–3d; Table S2). It was found that the Ca, Mg, and Si ion concentrations in all four groups increased in a similar trend, especially

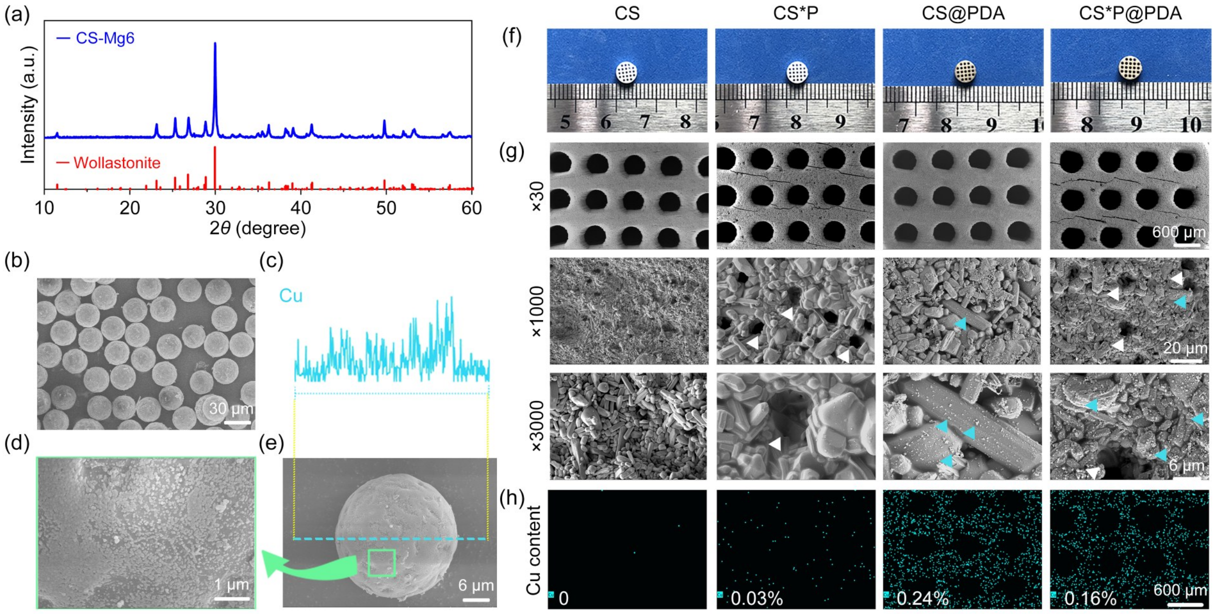

Fig. 2 Fabrication and validation of PDA(Cu^{2+})-modified scaffolds. (a) XRD analysis of CS-Mg6 powders. (b–e) SEM images of the PMMA with PDA(Cu^{2+}) nanoparticles; (c, e) the line-scanning EDX spectra of Cu distribution in the surface. Blue-dotted line: line-scanning range; green frame: area magnified in (d). (f) Macroscopic appearance of scaffolds with or without PDA(Cu^{2+}) modification. (g) SEM images of scaffolds under different magnifications. White arrows: micropores; blue arrows: PDA nanoparticles. (h) EDS mapping of Cu component at different mass fractions on the surface. XRD: X-ray diffraction; CS: calcium silicate; CS-Mg6: magnesium-doped CS; SEM: scanning electron microscopy; PMMA: polymethyl methacrylate; PDA: polydopamine; EDX: energy-dispersive X-ray; PDA(Cu^{2+}): copper-containing PDA; EDS: EDX spectroscopy; *P: internal modification; @PDA: external modification; *P@PDA: two-step internal/external modification.

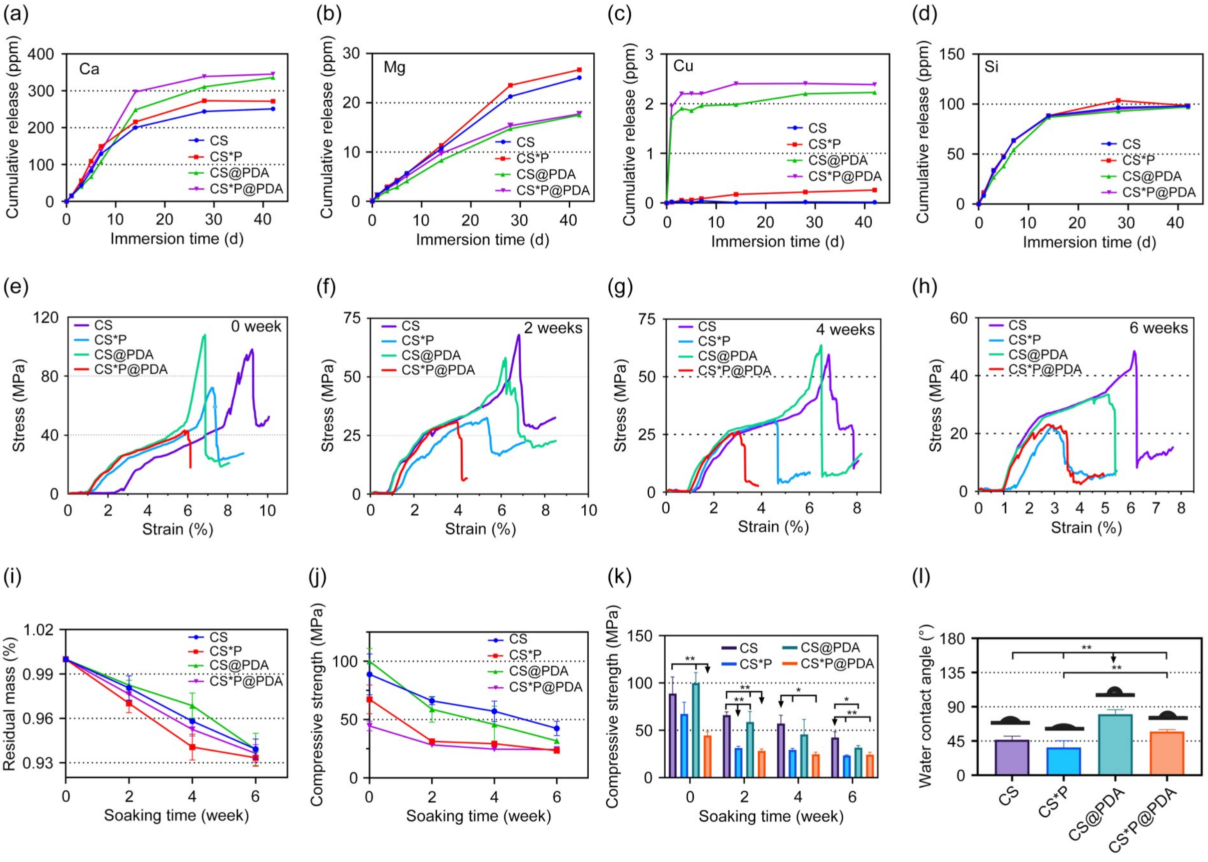

Fig. 3 Mechanics, biodegradability, and hydrophilic characterization of scaffolds with PDA(Cu^{2+}) modifications. (a–d) Changes in the cumulative releasing ion concentrations in Tris-buffer during immersion test. (e–k) Change rules of mass decrease (i) and compressive strength (e–h, j, k) of the scaffolds after soaking for 0, 2, 4, and 6 weeks. (l) The hydrophilicity of scaffolds. (i–l) The data were expressed as mean±standard deviation (*n*=6). * *P*<0.05, ** *P*<0.01, with the arrows indicating that the group pointed to has a significant difference compared with the other groups. CS: calcium silicate; PDA: polydopamine; PDA(Cu^{2+}): copper-containing PDA; *P: internal modification; @PDA: external modification; *P@PDA: two-step internal/external modification; ppm: $\times10^{-6}$ or mg/L.

Si ions. However, it was interesting that the external PDA(Cu^{2+}) modification accelerated the Ca^{2+} release, while it slowed down the Mg^{2+} release. In addition, the CS@PDA and CS*P@PDA scaffolds with external macropore modification showed relatively fast Cu^{2+} ion release in the initial 3 d, followed by gradually decreasing release rate and reaching a stable plateau of Cu^{2+} ion concentration. In contrast, internal micropore modification in the CS*P scaffolds displayed mild Cu^{2+} release in the whole immersion stage (Fig. 3c). As expected, the CS*P@PDA scaffolds exhibited the characteristics of both internal micropore and external macropore modification with Cu^{2+} ions, which means that Cu^{2+} ions had a special pattern of rapid release in the early stage and slow release in the late stage, consistent with the original design intention for these multifunctional scaffolds.

The scaffolds were subjected to a compressive resistance test before and after Tris immersion treatment to evaluate the mechanical evolution with time. As shown in Figs. 3e–3h, all scaffolds with different modifications exhibited a similar fracture behavior before and after immersion in aqueous medium. The compressive strengths of the CS and CS@PDA scaffolds were equal (100–110 MPa) and significantly higher than those of the CS*P@PDA scaffolds ((44.53±3.29) MPa). This indicated that the external PDA(Cu^{2+}) modification hardly changed the compressive strength of scaffolds, while the isolated micropores generated by internal modification could heavily affect the compressive resistance. With the prolongation of immersion time in Tris buffer, the scaffolds showed a steady mass loss and strength decay (Figs. 3i and 3j). In fact, the scaffolds in each group showed similar biodegradability (a mass loss of about 6% within six weeks), whereas the CS*P and CS*P@PDA scaffolds with internal modification exhibited a slightly higher mass loss. It was observed that the strength of all scaffolds decreased relatively quickly in the initial two weeks, and then maintained a steady decline during the next four weeks (Figs. 3j and 3k). It was also worth mentioning that the CS*P@PDA scaffolds exhibited considerable strength ((24.28±2.21) MPa) after six weeks of bio-dissolution.

The surface contact angle analysis revealed the hydrophilic property of bioceramic scaffolds before and after PDA(Cu^{2+}) modification. As shown in Fig. 3l, because of the surface microporous structures on the macropore struts, CS*P scaffolds could contribute more to hydrophilicity than the CS scaffolds; however, the external PDA(Cu^{2+}) modification could increase the surface contact angles of the CS@PDA and CS*P@PDA scaffolds, suggesting that the organic coating of PDA(Cu^{2+}) was more hydrophobic in comparison to the bioceramic surface.

3.4 In vitro validation of antibacterial effect

S. aureus and *E. coli*, typical Gram-positive and Gram-negative species of bacteria, respectively, were used to assess the antibacterial potential of the bioceramic scaffolds. As shown in Figs. 4a and 4b, the bacterial survival was reduced significantly in the CS@PDA and CS*P@PDA groups after incubating with *S. aureus* and *E. coli* for only 40 min, implying that an obvious contact-active antibacterial activity was triggered by the external PDA(Cu^{2+}) modification. Evidently, the bacteriostatic ability was correlated with the duration of external PDA(Cu^{2+}) modification. The CS*P scaffolds with internal modification were also endowed with a mild antibacterial potential. Figs. 4c and 4d exhibit quantitative plate count analyses, from which it can be found that the scaffolds with 2 h of external PDA(Cu^{2+}) modification could kill almost all of the bacteria. However, it seemed that the PDA(Cu^{2+}) showed a more potent antibacterial effect on Gram-positive bacteria.

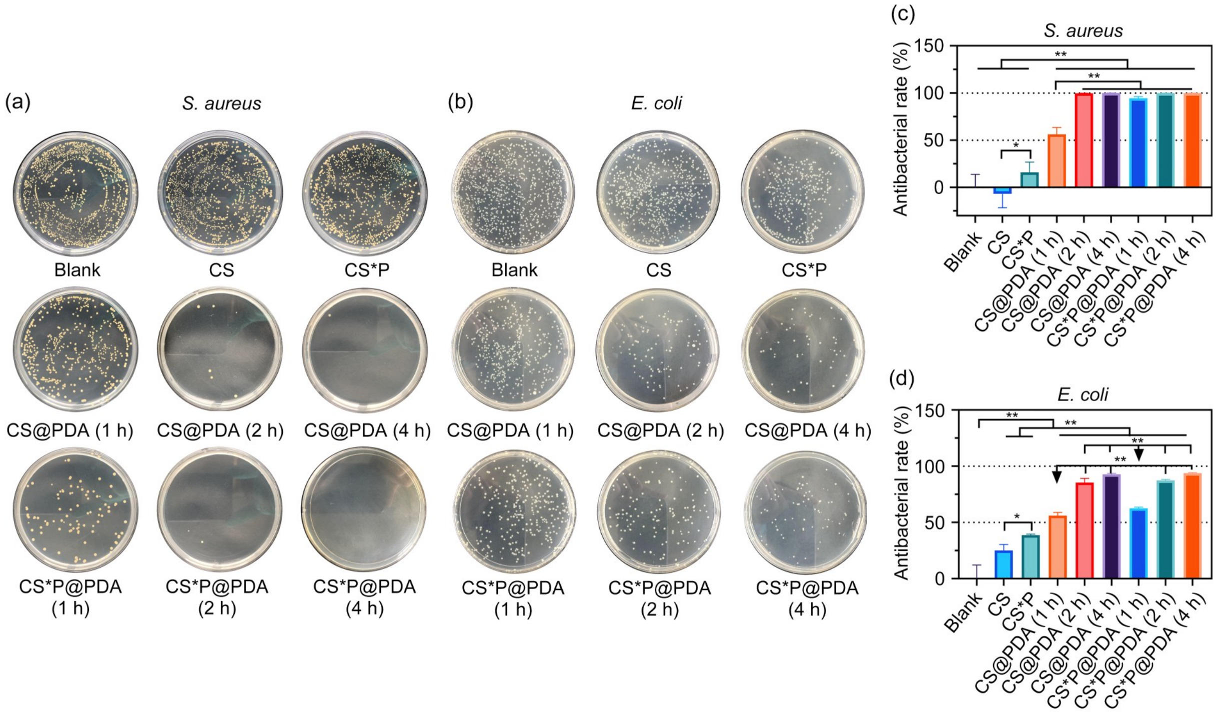

Fig. 4 Antibacterial performance of scaffolds in vitro. (a, b) Spread plate images of *Staphylococcus aureus* and *Escherichia coli*, respectively, after seeding on the scaffolds with or without modification for 40 min. (c, d) The quantitative outcomes of antibacterial capacity of *S. aureus* and *E. coli*, respectively. The data were expressed as mean±standard deviation (SD), *n*=6. * *P*<0.05, ** *P*<0.01, with the arrows indicating that the group pointed to has a significant difference compared with the other groups. CS: calcium silicate; PDA: polydopamine; *P: internal modification; @PDA: external modification; *P@PDA: two-step internal/external modification.

3.5 In vitro evaluation of the osteogenic ability of modified scaffolds

The primary OBs were selected to evaluate the osteogenic capability of the porous scaffolds in vitro. After treating the extract of scaffolds for 7 d, OBs in all groups presented significantly higher proliferative activity than those in the blank group (Figs. 5a and 5b). The live-dead double staining test provided further evidence that there was no obvious difference in fluorescence among the different scaffold groups and the blank group (Fig. 5c).

ALP staining and quantitative real-time PCR (qRT-PCR) analyses were performed to assess the osteogenic capacity of the prepared porous scaffolds. After being cultured for 7 and 14 d, OBs in all modified scaffold groups, especially in the CS*P group, exhibited greater ALP expression compared to the CS group (Fig. 5f). Meanwhile, the expression of osteogenesis-related genes, including Runt-related transcription factor 2 (*Runx2*), osteocalcin (*OC*), and type I collagen (*Col-I*), presented the most significant upregulation in the CS*P group (Figs. 5d and 5e), possibly due to its lower Cu^{2+} dosage in the culture medium. Moreover, the other two groups of CS@PDA and CS*P@PDA with external PDA(Cu^{2+}) modification also showed enhancement in the expression levels of such osteogenic genes.

3.6 In vitro evaluation of the angiogenic ability of modified scaffolds

Next, we evaluated the angiogenic ability of modified scaffolds with HUVECs in vitro. As expected, the PDA(Cu^{2+}) modification exhibited a good cytocompatibility in the HUVEC culture (Figs. 6a and 6b). In the initial 3 d of culture, HUVECs in the scaffold groups showed a significantly greater proliferation activity than

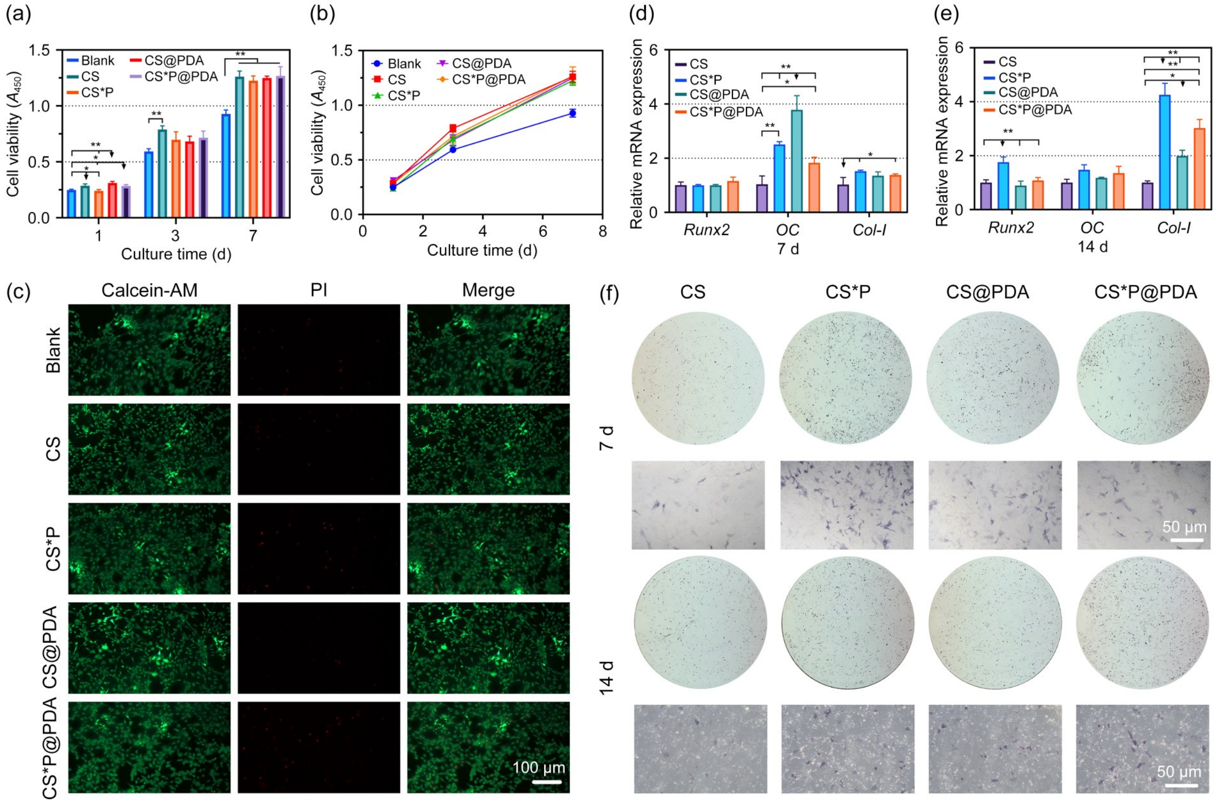

Fig. 5 Proliferation and osteogenesis of OBs cultured with the extract of scaffolds. (a, b) CCK-8 results and proliferation curves of OBs cultured for 1, 3, and 7 d. (c) Fluorescent images of OBs cultured for 1 d. (d, e) Relative osteogenic-specific mRNA expression of OBs cultured for 7 and 14 d: *Runx2*, *OC*, and *Col-I*. (f) ALP staining of OBs cultured for 7 and 14 d. The data were expressed as mean±standard deviation (SD), *n*=6. * *P*<0.05, ** *P*<0.01, with the arrows indicating that the group pointed to has a significant difference compared with the other groups. OBs: osteoblasts; CCK-8: cell counting kit-8; mRNA: messenger RNA; *Runx2*: Runt-related transcription factor 2; *OC*: osteocalcin; *Col-I*: type I collagen; ALP: alkaline phosphatase; CS: calcium silicate; PDA: polydopamine; *P: internal modification; @PDA: external modification; *P@PDA: two-step internal/external modification; A_{450}: absorbance at 450 nm; AM: acetoxymethyl ester; PI: propidium iodide.

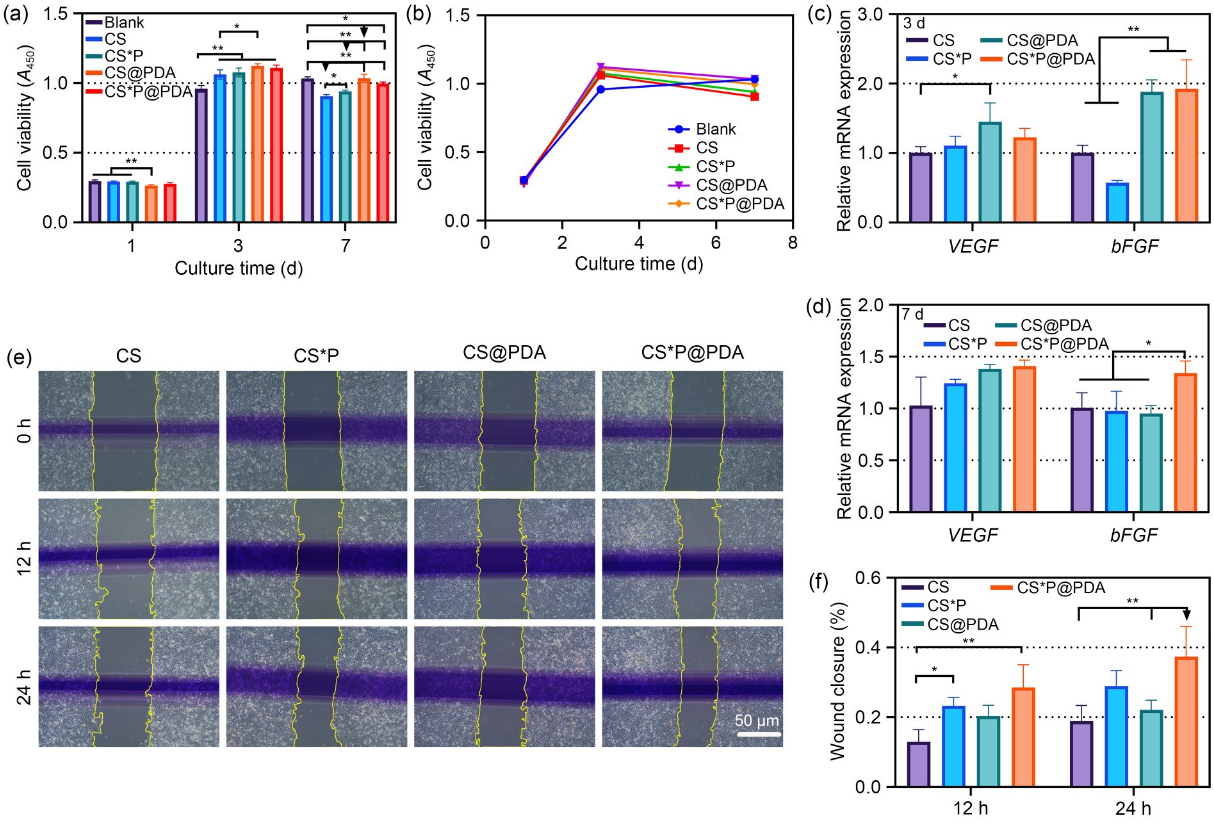

Fig. 6 Proliferation and angiogenesis of HUVECs cultured with the extract of scaffolds. (a, b) CCK-8 results of HUVECs cultured for 1, 3, and 7 d. (c, d) Relative angiogenic-specific mRNA expression of HUVECs cultured for 3 and 7 d: *VEGF* and *bFGF*. (e) HUVEC scratch-wound migration assay. (f) Quantification of wound healing. The data were expressed as mean±standard deviation (SD), *n*=6. * *P*<0.05, ** *P*<0.01, with the arrows indicating that the group pointed to has a significant difference compared with the other groups. HUVECs: human umbilical vein endothelial cells; CCK-8: cell counting kit-8; mRNA: messenger RNA; *VEGF*: vascular endothelial growth factor; *bFGF*: basic fibroblast growth factor; CS: calcium silicate; PDA: polydopamine; *P: internal modification; @PDA: external modification; *P@PDA: two-step internal/external modification; A_{450}: absorbance at 450 nm.

those in the blank group. In particular, the activity of HUVECs in the scaffold groups was inferior to that in the blank group after 7 d, which may be due to the oversaturation of cell density. As for the angiogenic potential analysis, the CS*P@PDA group showed the greatest capacity to promote endothelial cell migration through the scratch assay (Fig. 6e), and the quantitative results indicated that this was significantly higher compared to the CS group (*P*<0.05; Fig. 6f). As a matter of fact, the expression of angiogenesis-related genes displayed similar results. As shown in Figs. 6c and 6d, the CS*P@PDA group possessed the most abundant basic fibroblast growth factor (*bFGF*) expression after 3 and 7 d of culture, with a statistical difference (*P*<0.05) in comparison with the CS group. In addition, it was noted that the modified scaffold groups still brought out a tendency of enhancement in vascular endothelial growth factor (*VEGF*) expression.

3.7 μCT reconstruction analysis of bone repair in vivo

Early-stage bone regeneration in the porous scaffolds was evaluated in vivo after implantation into the mandibular defect for four weeks. No rabbits showed obvious infection, and all of them survived to the point of specimen harvest. According to the gross examination shown in Fig. 7a, new tissues were obviously extending into the bone defect in all groups. The scaffolds were tightly integrated with the host bone tissue in the CS and CS*P@PDA groups, indicating the good compatibility of scaffolds. As for the blank group, although bone tissue ingrowth was detected in the defect area, distinct concave areas were observed

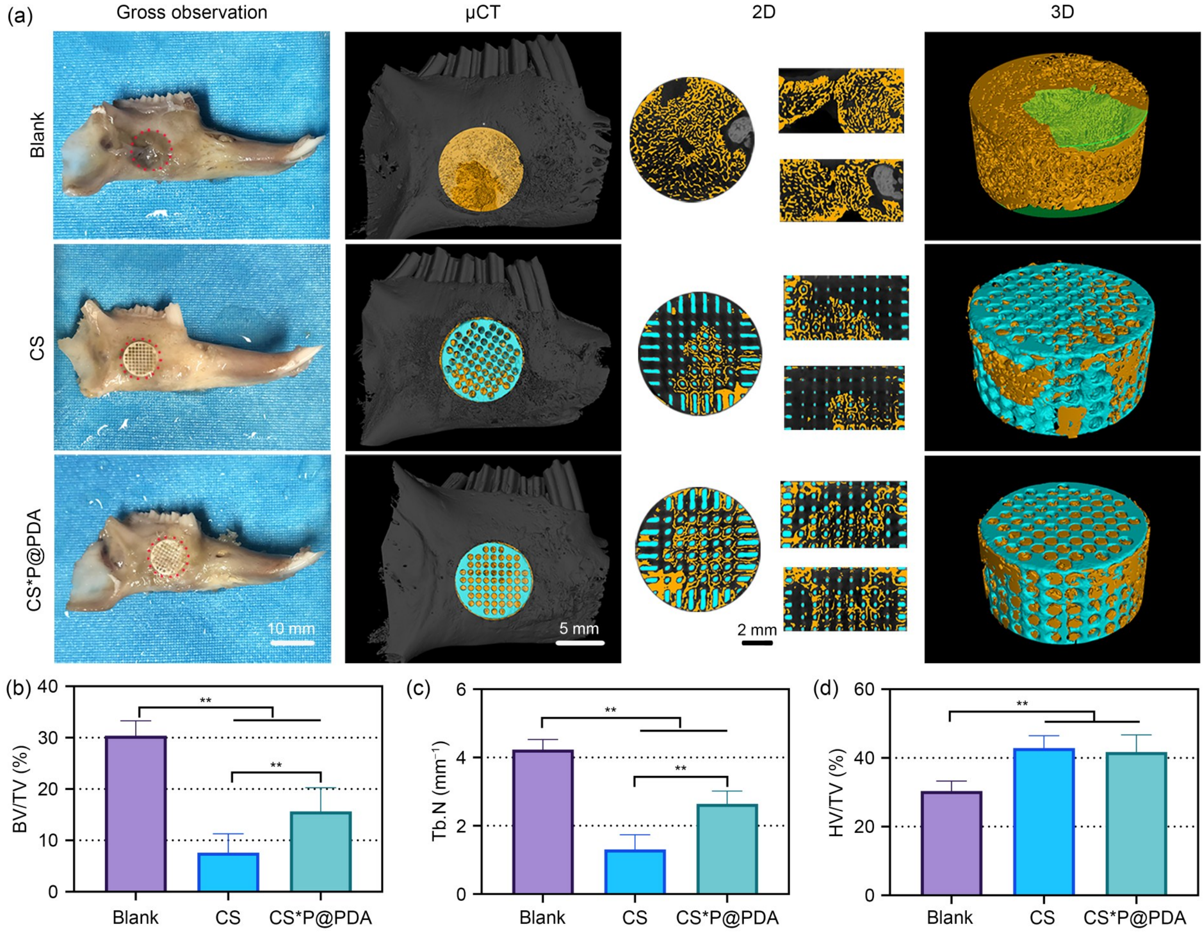

Fig. 7 Early osteogenic effect of scaffolds in vivo. (a) µCT construction of implant samples at four weeks post-operation. Red dotted circle: bone defect area; Blue: scaffolds; Yellow: neo-bone tissue; Green: bone depression. (b–d) Quantitative analysis of osteogenic capacity: newly formed BV/TV (b), Tb.N (c), and HV/TV (d). The HV is equal to the sum of residual scaffold volume and newly formed BV. The data were expressed as mean±standard deviation (SD), *n*=6. ** *P*<0.01. µCT: microcomputed tomography; BV: bone volume; TV: total volume; Tb.N: trabecular number; HV: hard tissue volume; CS: calcium silicate; PDA: polydopamine; *P: internal modification; @PDA: external modification; *P@PDA: two-step internal/external modification.

directly on the surface, reflecting the essential role of the regeneration space laterally supported by the scaffolds.

The µCT reconstruction images showed that a large amount of new bone tissues grew into the defect of the blank group, although there were two collapses without the tendency of bone regeneration. In contrast, the implants in the two scaffold groups still kept a good structural stability at four weeks, and provided porous substrate for the ingrowth of new bone tissue. The 3D section analysis of the bone defects indicated that the new bone tissue grew from the periphery of the scaffold along the pore to the center. Among them, this tissue in the CS group only occupied part of the space of the scaffold pores, whereas the modified CS*P@PDA group showed a significant superior bone regeneration response, and the new bone in all directions had reached the center of the scaffold, suggesting the considerable osteostimulatory effect of the PDA(Cu^{2+}) modification on the bone defects.

Furthermore, the quantitative analysis of new bone formation was shown in Figs. 7b–7d. The newly formed bone (BV/TV) and trabecular bone density (Tb.N) in the CS* P@PDA group were significantly higher than those in the CS group, which were consistent with the observation of 3D reconstruction. Additionally, the blank group presented higher BV/TV and Tb.N than the scaffold groups, which may be attributed to the body's own early-stage regenerative potential in the mandibular bone defect.

3.8 Histological analysis of the bone repair in vivo

The bone specimens were further subjected to histological analysis by HE staining and MacNeal staining (Fig. 8). After four weeks, part of the drilled area in the blank group indicated a significant repair effect with intensive trabeculae, but it cannot be ignored that there was still a large defect without any tissue, showing no indication of repair (Figs. 8a and 8d). Based on the HE staining images, the porous architectures were still maintained after four weeks of scaffold implantation, and the scaffolds of both groups were well integrated with the surrounding tissues and there was no obvious inflammatory reaction (Figs. 8b2 and 8c2). The growth of newly formed bone tissue could be seen in the macropores at the edge of the scaffolds in both the CS and CS*P@PDA groups, while the difference was that the quantity of newly formed bone in the central region of CS*P@PDA scaffolds was significantly better. Moreover, the MacNeal staining of sections (Fig. 8i) showed that the bone tissue tended to extend from the edge of the scaffolds to the centre region. The bone growth rate in the CS group was slower compared to the CS*P@PDA group, and most of the newly formed bone remained at the edge of the scaffolds. By contrast, in the CS*P@PDA group, the newly formed bone was evenly distributed in the scaffolds, in which the amount of bone tissue was significantly more than that in the CS group (Figs. 8e1, 8e2, 8f1, and 8f2), which confirmed the outstanding pro-osteogenic capability in the early stage brought about by the internal modification of PDA(Cu^{2+}). In addition, a quantitative analysis was performed on the proportion of new bone within the drilled area, and the results showed that it was significantly higher in the CS*P@PDA group than in the CS group, but the difference compared to the blank group was not statistically significant (Fig. 8j).

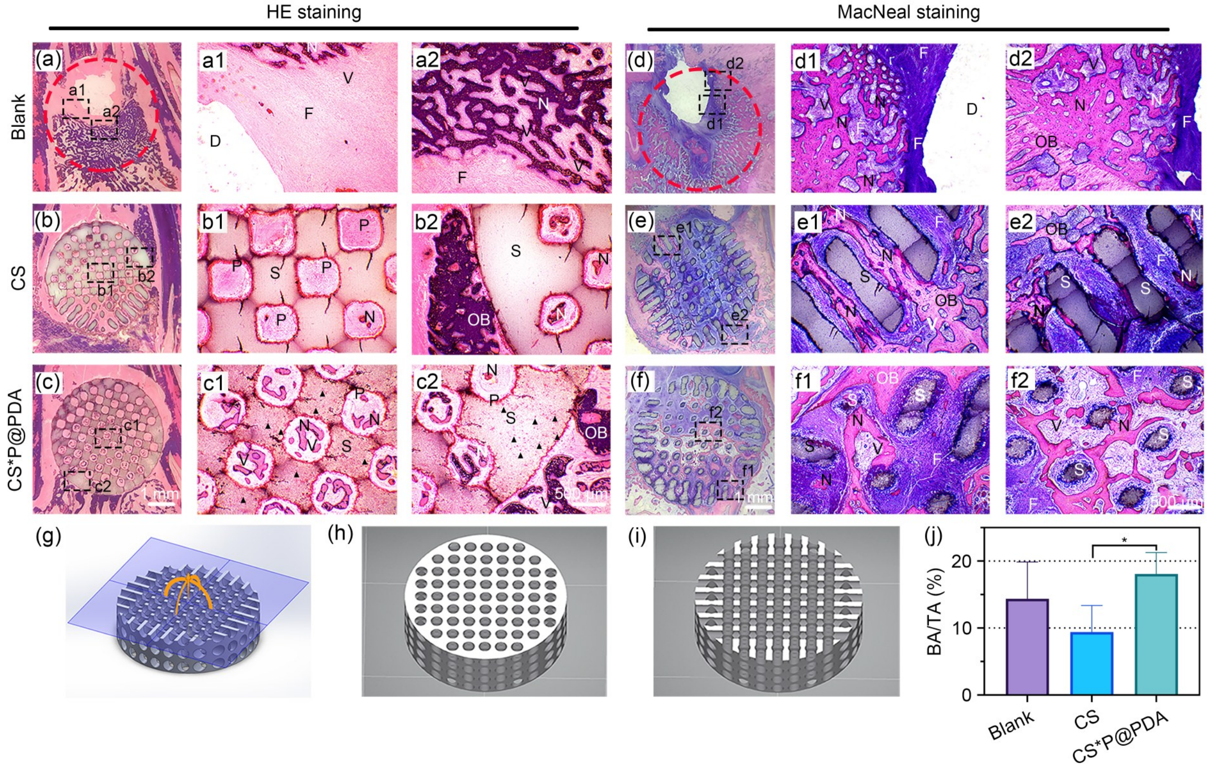

Fig. 8 Histological observation (HE and MacNeal staining) of the early osteogenic effect after four weeks of scaffold implantation. Transverse sections observed at low (a–f, 15×) and high (a1–f1 and a2–f2, 40×) magnifications. Red dotted circle: drilled area; Black dotted frame: enlarged area; Solid arrow: surface pit; D: defect; F: fiber; V: vessel; N: newly formed bone; P: pore; S: scaffold; OB: original bone. (g–i) Schematic diagrams of different scaffold sections: (h) the section is consistent with HE staining; (i) the section is consistent with MacNeal staining. (j) Quantitative analysis of the newly formed bone area (BA)/total area (TA) by MacNeal staining. The data were expressed as mean±standard deviation (SD), *n*=6. * $P<0.05$. HE: hematoxylin/eosin; MacNeal: tetrachrome stain; CS: calcium silicate; PDA: polydopamine; *P: internal modification; @PDA: external modification; *P@PDA: two-step internal/external modification.

4 Discussion

Nowadays, the clinical application of granular bone graft materials is limited by the disadvantages of shaping difficulty, tendency for displacement, and poor mechanical properties (Jung et al., 2011; Lei et al., 2020b). The 3D-printed bioceramic scaffolds proposed in our previous studies have overcome these difficulties well (Wu et al., 2021; Lu et al., 2023). However, another clinical problem has emerged that the incidence of infections after operation ranges from 2% to 11% (Sanz-Sánchez et al., 2022), and these undesired events ultimately impair bone regeneration or even lead to operation failure. To cope with the complex oral bacterial milieu, in addition to the routine clinical use of antibacterial mouthwashes, the ability of implants to resist infection has attracted growing attention. In this study, we pioneered the use of PDA(Cu^{2+}) rapid deposition method to fabricate 3D bioceramic scaffolds with multiple functions via two-step modification, endowing them with early-stage antibacterial properties through external modification and improving their osteogenic capacity through internal modification.

Some studies have used dopamine to form PDA coating and substrate modification through oxidative self-polymerization (Lee et al., 2007; Su et al., 2022). This process is facile but lowly efficient. Zhang et al. (2016) used H_2O_2 and copper ions as catalysts to realize the rapid polymerization of dopamine, and copper ions were simultaneously chelated in PDA. We employed this new approach to modify the CS-Mg6 bioceramic scaffold within 1 h (Figs. 2f and 2g). The deep color on the scaffold (Fig. 2f) indicated the new PDA(Cu^{2+}) modification layer, and the color deepened with the prolongation of treatment time. On the other hand, copper ions have been widely studied in biomedical devices because of their potent broad-spectrum antibacterial potential and low drug resistance (Liu ZY et al., 2016; Xiao et al., 2018). The antibacterial mechanism of copper ions mainly includes two aspects: first, direct contact between copper ions and bacteria may destroy the integrity of their cell membrane (Hong et al., 2012; Santo et al., 2012); second, the dissociative copper ions can trigger the generation of reactive oxygen species (ROS), inhibiting cellular respiration and leading to bacterial DNA degradation (Santo et al., 2008; Warnes and Keevil, 2011). This antibacterial effect can be achieved in the early stage of scaffold implantation through the release of copper ions from the PDA(Cu^{2+}) coating.

In our study, the externally modified coating presented rapid copper ion release within the initial few days (Fig. 3c). In the antibacterial tests in vitro, the CS@PDA and CS*P@PDA scaffolds showed appreciable antibacterial responses against *S. aureus* and *E. coli*. Notably, a longer modification time could produce a stronger on-contact antibacterial capability (Figs. 4a and 4b). This result means that a higher density of surface phenolic hydroxyl groups and more copper ions can eventually lead to a higher release rate of copper ions (Zhou et al., 2020). Thus, the modification time can tune the amount of copper ion chelation and even the on-contact antibacterial activity. Meanwhile, PDA itself is characterized by the activity of generating ROS through redox reactions, and thus can also achieve an antibacterial effect (Liu et al., 2019). PDA(Cu^{2+}) modification plays a synergistic antibacterial role (Lin et al., 2021), and this may help to reduce the requirement of copper ion dosage. From this aspect, our OB and HUVEC culture tests in vitro confirmed the cytocompatibility of this external coating layer (Figs. 5 and 6).

In order to enhance the osteogenic capability of CS-Mg6 scaffolds, we also proposed an internal modification strategy using PDA(Cu^{2+})-modified PMMA microspheres as a porogen in the bioceramic struts of scaffolds. The addition of such PDA(Cu^{2+})-modified PMMA to the printing slurry is thought to reduce the potential adverse effect of bioceramic sintering. Moreover, the PMMA microspheres can contribute to the formation of many micropores after sintering, which may be favorable for tailing the surface and internal microstructure of the bioceramic struts (Fig. 2g). On the one hand, the microporous structure in the scaffold will increase the specific surface area, thereby accelerating the degradation rate of the scaffold and improving the degradation performance of the CS scaffold, to better match the regeneration rate of bone tissue (Fig. S2). On the other hand, previous studies have indicated that the surface hydrophilicity of the biomaterial can adjust the adhesion, migration, and differentiation of osteogenic cells (Bang et al., 2014; Zhao et al., 2014; Nemţoi et al., 2017). The phenolic hydroxyl and amino groups in the PDA coating are hydrophilic, whereas the hydrophilicity of CS@PDA was lower than that of the pure CS-Mg6 scaffolds. In contrast, the microporous structure derived from the internal modification in the

CS*P@PDA scaffold might contribute to the hydrophilicity (Fig. 3l). In fact, previous studies have shown that the surface roughness at the micron-, submicron-, and nano-levels could facilitate OB differentiation and local factor production (Gittens et al., 2011; Steeves et al., 2016; Kaushik et al., 2020), which coincides with the surface morphology of the CS*P@PDA scaffold.

Research has demonstrated that low concentrations of copper ions enhance the proliferation and activity of endothelial cells and OBs (Ewald et al., 2012; Kong et al., 2014), and their combination with biomaterials can help improve microvascular formation and bone regeneration in vivo (Gao et al., 2021; Li et al., 2022). Our in vitro experiments indicated that both the CS*P@PDA and CS*P scaffolds exhibited more excellent angiogenic and osteogenic capacities in comparison with the CS scaffolds (Figs. 5 and 6). It is well accepted that rapid vascularization is key to promote osseointegration and bone regeneration (Filipowska et al., 2017), as the fibrovascular networks can provide sufficient nutrients. In the early stage, the CS*P@PDA scaffold exhibited the best angiogenic effect. With the degradation of surface modification, the scaffold evolved into CS*P, which exerted a long-lasting osteogenic effect. In our animal model experiment in vivo, the CS*P@PDA showed appreciable new bone formation, and more neovascularization was found in the stained tissue sections within four weeks (Figs. 7 and 8). Although the blank group exhibited considerable bone tissue regeneration in rabbit mandibular defects in the early stage, the lack of scaffold support to maintain space ultimately resulted in the presence of remaining unhealable bone defect pits in this group (Figs. 7a, 8a, and 8d). Similarly, in periodontal treatment, a permanent reduction in the alveolar bone height was unexpected (Qin et al., 2022). Hence, the porous scaffold is recognized to provide space and substrate for new bone tissue ingrowth while avoiding the inefficient bone tissue remodeling.

Overall, the PDA(Cu^{2+}) modification strategy was demonstrated to provide a simple and effective option for enhancing the biological performances of conventional bioceramic scaffolds. The two-step PDA(Cu^{2+}) modification of bioceramic scaffolds satisfied several functional requirements in different stages of bone repair. As such, we demonstrated the feasibility of this technology in endowing bioceramic scaffolds with desirable properties. However, our study still has limitations. Firstly, the optimal modification conditions need to be comprehensively validated to reach a balance between antibacterial and osteogenic effects. Moreover, the in vivo tests in this study only evaluated the early-stage osteogenesis, while the effects of the proposed method on long-term bone regeneration and repair should be confirmed in future work.

5 Conclusions

In summary, using a unique two-step PDA(Cu^{2+}) modification technology in 3D-printed bioceramic scaffolds, PDA(Cu^{2+}) dually-modified bioceramic scaffolds were prepared, and their physicochemical, antibacterial, osteogenic, and angiogenic properties were systematically evaluated. It was demonstrated that the dually modified CS*P@PDA scaffold achieved superior antibacterial potential, angiogenesis, and osteogenesis compared with the CS scaffold. Our facile and versatile PDA(Cu^{2+}) dual modification strategy provides a flexibility in optimizing the physicochemical properties and biological performances of bioceramic scaffolds. It is reasonable to consider that such 3D-printed bioceramic scaffolds with two-step PDA(Cu^{2+}) modification are promising candidates to develop multifunctional bioceramic scaffolds with personalized morphology for matching with alveolar bone defects under diverse clinical pathological scenarios.

Data availability statement

All statistical data supporting the findings of this study are available from the corresponding author upon reasonable request.

Acknowledgments

This work was supported by the Key Research and Development Program of Zhejiang Province Foundation (No. 2019C03027), the Zhejiang Provincial Natural Science Foundation of China (No. LZ22E020002), the Scientific Research Fund of Zhejiang Provincial Education Department (No. Y202148333), and the Zhejiang Provincial Basic Research for Public Welfare Funds (Nos. LGF22E030002, LGF21H140001, and LTGY23H140005), China. We thank Dr. Wangsiyuan TENG (Zhejiang University, Hangzhou, China) for his friendly provision of *S. aureus* and *E. coli* and Dr. Yuting YANG (Zhejiang University) for her kindly donation of HUVECs.

Author contributions

Xiaojian JIANG: conceptualization, writing – original draft, data curation, and formal analysis; Lihong LEI: funding

acquisition and resources; Weilian SUN: funding acquisition and resources. Yingming WEI: methodology and writing – reviewing and editing; Jiayin HAN: methodology; Shuaiqi ZHONG: visualization; Xianyan YANG: methodology and funding acquisition; Zhongru GOU: conceptualization, writing – review and editing, funding acquisition, and supervision; Lili CHEN: conceptualization, resources, project administration, and funding acquisition. All authors have read and approved the final manuscript, and therefore, have full access to all the data in the study and take responsibility for the integrity and security of the data.

Compliance with ethics guidelines

Xiaojian JIANG, Lihong LEI, Weilian SUN, Yingming WEI, Jiayin HAN, Shuaiqi ZHONG, Xianyan YANG, Zhongru GOU, and Lili CHEN declare that they have no conflict of interest.

All the animal procedures were approved by the Zhejiang University Ethics Committee, Hangzhou, China (No. ZJU20220139) and the Ethics Committee of the Second Affiliated Hospital, Zhejiang University School of Medicine, Hangzhou, China (No. AIRB-2021-382).

References

Bang SM, Moon HJ, Kwon YD, et al., 2014. Osteoblastic and osteoclastic differentiation on SLA and hydrophilic modified SLA titanium surfaces. *Clin Oral Implants Res*, 25(7): 831-837.
https://doi.org/10.1111/clr.12146

de Almeida MS, de Oliveira Fernandes GV, de Oliveira AM, et al., 2018. Calcium silicate as a graft material for bone fractures: a systematic review. *J Int Med Res*, 46(7):2537-2548.
https://doi.org/10.1177/0300060518770940

de Azambuja Carvalho PH, dos Santos Trento G, Moura LB, et al., 2019. Horizontal ridge augmentation using xenogenous bone graft—systematic review. *Oral Maxillofac Surg*, 23(3):271-279.
https://doi.org/10.1007/s10006-019-00777-y

Dong YF, Duan HB, Zhao NR, et al., 2018. Three-dimensional printing of β-tricalcium phosphate/calcium silicate composite scaffolds for bone tissue engineering. *Bio-Des Manuf*, 1(2):146-156.
https://doi.org/10.1007/s42242-018-0010-5

Doolittle ML, Ackert-Bicknell CL, Jonason JH, 2021. Isolation and culture of neonatal mouse calvarial osteoblasts. *In*: Hilton MJ (Ed.), Skeletal Development and Repair. Humana, New York, p.425-436.
https://doi.org/10.1007/978-1-0716-1028-2_26

Ewald A, Käppel C, Vorndran E, et al., 2012. The effect of Cu(II)-loaded brushite scaffolds on growth and activity of osteoblastic cells. *J Biomed Mater Res Part A*, 100A(9):2392-2400.
https://doi.org/10.1002/jbm.a.34184

Fan YJ, Pham MT, Huang CJ, 2019. Development of antimicrobial and antifouling universal coating via rapid deposition of polydopamine and zwitterionization. *Langmuir*, 35(5):1642-1651.
https://doi.org/10.1021/acs.langmuir.8b01730

Filipowska J, Tomaszewski KA, Niedźwiedzki Ł, et al., 2017. The role of vasculature in bone development, regeneration and proper systemic functioning. *Angiogenesis*, 20(3):291-302.
https://doi.org/10.1007/s10456-017-9541-1

Gao XY, Wei MT, Ma DC, et al., 2021. Engineering of a hollow-structured $Cu_{2-x}S$ nano-homojunction platform for near infrared-triggered infected wound healing and cancer therapy. *Adv Funct Mater*, 31(52):2106700.
https://doi.org/10.1002/adfm.202106700

Gittens RA, McLachlan T, Olivares-Navarrete R, et al., 2011. The effects of combined micron-/submicron-scale surface roughness and nanoscale features on cell proliferation and differentiation. *Biomaterials*, 32(13):3395-3403.
https://doi.org/10.1016/j.biomaterials.2011.01.029

Hong R, Kang TY, Michels CA, et al., 2012. Membrane lipid peroxidation in copper alloy-mediated contact killing of *Escherichia coli*. *Appl Environ Microbiol*, 78(6):1776-1784.
https://doi.org/10.1128/aem.07068-11

Hou YH, Wang WG, Bartolo P, 2022. Application of additively manufactured 3D scaffolds for bone cancer treatment: a review. *Bio-Des Manuf*, 5(3):556-579.
https://doi.org/10.1007/s42242-022-00182-7

Hu JF, Yang L, Yang P, et al., 2020. Polydopamine free radical scavengers. *Biomater Sci*, 8(18):4940-4950.
https://doi.org/10.1039/d0bm01070g

International Organization for Standardization, 2012. Biological evaluation of medical devices—Part 12: Sample preparation and reference materials. ISO 10993-12:2012. International Organization for Standardization, Switzerland.

Jung UW, Lee JS, Park WY, et al., 2011. Periodontal regenerative effect of a bovine hydroxyapatite/collagen block in one-wall intrabony defects in dogs: a histometric analysis. *J Periodontal Implant Sci*, 41(6):285-292.
https://doi.org/10.5051/jpis.2011.41.6.285

Kassebaum NJ, Bernabé E, Dahiya M, et al., 2014. Global burden of severe periodontitis in 1990–2010: a systematic review and meta-regression. *J Dent Res*, 93(11):1045-1053.
https://doi.org/10.1177/0022034514552491

Kaushik N, Nhat Nguyen L, Kim JH, et al., 2020. Strategies for using polydopamine to induce biomineralization of hydroxyapatite on implant materials for bone tissue engineering. *Int J Mol Sci*, 21(18):6544.
https://doi.org/10.3390/ijms21186544

Kim Y, Nowzari H, Rich SK, 2013. Risk of prion disease transmission through bovine-derived bone substitutes: a systematic review. *Clin Implant Dent Relat Res*, 15(5):645-653.
https://doi.org/10.1111/j.1708-8208.2011.00407.x

Kong N, Lin KL, Li HY, et al., 2014. Synergy effects of copper and silicon ions on stimulation of vascularization by copper-doped calcium silicate. *J Mater Chem B*, 2(8):1100-1110.
https://doi.org/10.1039/c3tb21529f

Lee H, Dellatore SM, Miller WM, et al., 2007. Mussel-inspired surface chemistry for multifunctional coatings. *Science*, 318(5849):426-430.

https://doi.org/10.1126/science.1147241

Lei LH, Yu YY, Ke T, et al., 2019. The application of three-dimensional printing model and platelet-rich fibrin technology in guided tissue regeneration surgery for severe bone defects. *J Oral Implantol*, 45(1):35-43. https://doi.org/10.1563/aaid-joi-D-17-00231

Lei LH, Han JY, Wen JH, et al., 2020a. Biphasic ceramic biomaterials with tunable spatiotemporal evolution for highly efficient alveolar bone repair. *J Mater Chem B*, 8(35): 8037-8049. https://doi.org/10.1039/d0tb01447h

Lei LH, Wei YM, Wang ZX, et al., 2020b. Core-shell bioactive ceramic robocasting: tuning component distribution beneficial for highly efficient alveolar bone regeneration and repair. *ACS Biomater Sci Eng*, 6(4):2376-2387. https://doi.org/10.1021/acsbiomaterials.0c00152

Li B, Shu R, Dai WY, et al., 2022. Bioheterojunction-engineered polyetheretherketone implants with diabetic infectious micromilieu twin-engine powered disinfection for boosted osteogenicity. *Small*, 18(45):2203619. https://doi.org/10.1002/smll.202203619

Lin ZJ, Liu LZ, Wang W, et al., 2021. The role and mechanism of polydopamine and cuttlefish ink melanin carrying copper ion nanoparticles in antibacterial properties and promoting wound healing. *Biomater Sci*, 9(17):5951-5964. https://doi.org/10.1039/d1bm00622c

Liu A, Sun M, Shao HF, et al., 2016. The outstanding mechanical response and bone regeneration capacity of robocast dilute magnesium-doped wollastonite scaffolds in critical size bone defects. *J Mater Chem B*, 4(22):3945-3958. https://doi.org/10.1039/c6tb00449k

Liu H, Qu X, Tan HQ, et al., 2019. Role of polydopamine's redox-activity on its pro-oxidant, radical-scavenging, and antimicrobial activities. *Acta Biomater*, 88:181-196. https://doi.org/10.1016/j.actbio.2019.02.032

Liu ZY, Hu YX, Liu CF, et al., 2016. Surface-independent one-pot chelation of copper ions onto filtration membranes to provide antibacterial properties. *Chem Commun*, 52(82): 12245-12248. https://doi.org/10.1039/c6cc06015c

Lu WY, Shi Y, Xie ZJ, 2023. Novel structural designs of 3D-printed osteogenic graft for rapid angiogenesis. *Bio-Des Manuf*, 6(1):51-73. https://doi.org/10.1007/s42242-022-00212-4

Mertens C, Braun S, Krisam J, et al., 2019. The influence of wound closure on graft stability: an in vitro comparison of different bone grafting techniques for the treatment of one-wall horizontal bone defects. *Clin Implant Dent Relat Res*, 21(2):284-291. https://doi.org/10.1111/cid.12728

Nemţoi A, Trandafir V, Paşca AS, et al., 2017. Osseointegration of chemically modified sandblasted and acid-etched titanium implant surface in diabetic rats: a histological and scanning electron microscopy study. *Rom J Morphol Embryol*, 58(3): 881-886.

Qin HL, Wei YM, Han JY, et al., 2022. 3D printed bioceramic scaffolds: adjusting pore dimension is beneficial for mandibular bone defects repair. *J Tissue Eng Regen Med*, 16(4): 409-421. https://doi.org/10.1002/term.3287

Santo CE, Taudte N, Nies DH, et al., 2008. Contribution of copper ion resistance to survival of *Escherichia coli* on metallic copper surfaces. *Appl Environ Microbiol*, 74(4): 977-986. https://doi.org/10.1128/aem.01938-07

Santo CE, Quaranta D, Grass G, 2012. Antimicrobial metallic copper surfaces kill *Staphylococcus haemolyticus* via membrane damage. *MicrobiologyOpen*, 1(1):46-52. https://doi.org/10.1002/mbo3.2

Sanz-Sánchez I, Sanz-Martín I, Ortiz-Vigón A, et al., 2022. Complications in bone-grafting procedures: classification and management. *Periodontol 2000*, 88(1):86-102. https://doi.org/10.1111/prd.12413

Steeves AJ, Atwal A, Schock SC, et al., 2016. Evaluation of the direct effects of poly(dopamine) on the *in vitro* response of human osteoblastic cells. *J Mater Chem B*, 4(18):3145-3156. https://doi.org/10.1039/c5tb02510a

Su TS, Zheng A, Cao LY, et al., 2022. Adhesion-enhancing coating embedded with osteogenesis-promoting PDA/HA nanoparticles for peri-implant soft tissue sealing and osseointegration. *Bio-Des Manuf*, 5(2):233-248. https://doi.org/10.1007/s42242-022-00184-5

Sun M, Liu A, Shao HF, et al., 2016. Systematical evaluation of mechanically strong 3D printed diluted magnesium doping wollastonite scaffolds on osteogenic capacity in rabbit calvarial defects. *Sci Rep*, 6:34029. https://doi.org/10.1038/srep34029

Sun XY, Li LH, Zhang H, et al., 2021. Near-infrared light-regulated drug-food homologous bioactive molecules and photothermal collaborative precise antibacterial therapy nanoplatform with controlled release property. *Adv Healthc Mater*, 10(16):2100546. https://doi.org/10.1002/adhm.202100546

Wang XJ, Molino BZ, Pitkänen S, et al., 2019. 3D scaffolds of polycaprolactone/copper-doped bioactive glass: architecture engineering with additive manufacturing and cellular assessments in a coculture of bone marrow stem cells and endothelial cells. *ACS Biomater Sci Eng*, 5(9):4496-4510. https://doi.org/10.1021/acsbiomaterials.9b00105

Wang XL, Liu SX, Li M, et al., 2016. The synergistic antibacterial activity and mechanism of multicomponent metal ions-containing aqueous solutions against *Staphylococcus aureus*. *J Inorg Biochem*, 163:214-220. https://doi.org/10.1016/j.jinorgbio.2016.07.019

Warnes SL, Keevil CW, 2011. Mechanism of copper surface toxicity in vancomycin-resistant enterococci following wet or dry surface contact. *Appl Environ Microbiol*, 77(17): 6049-6059. https://doi.org/10.1128/aem.00597-11

Wei YM, Wang ZX, Han JY, et al., 2022. Modularized bioceramic scaffold/hydrogel membrane hierarchical architecture beneficial for periodontal tissue regeneration in dogs. *Biomater Res*, 26:68. https://doi.org/10.1186/s40824-022-00315-0

Wojcieszak D, Mazur M, Kalisz M, et al., 2017. Influence of Cu, Au and Ag on structural and surface properties of bioactive coatings based on titanium. *Mater Sci Eng C*, 71:1115-1121.
https://doi.org/10.1016/j.msec.2016.11.091

Wu CT, Zhou YH, Xu MC, et al., 2013. Copper-containing mesoporous bioactive glass scaffolds with multifunctional properties of angiogenesis capacity, osteostimulation and antibacterial activity. *Biomaterials*, 34(2):422-433.
https://doi.org/10.1016/j.biomaterials.2012.09.066

Wu RH, Li YF, Shen MD, et al., 2021. Bone tissue regeneration: the role of finely tuned pore architecture of bioactive scaffolds before clinical translation. *Bioact Mater*, 6(5): 1242-1254.
https://doi.org/10.1016/j.bioactmat.2020.11.003

Xiao YQ, Cao YJ, Xin BJ, et al., 2018. Fabrication and characterization of electrospun cellulose/polyacrylonitrile nanofibers with Cu(II) ions. *Cellulose*, 25(5):2955-2963.
https://doi.org/10.1007/s10570-018-1784-5

Xie JJ, Yang XY, Shao HF, et al., 2016. Simultaneous mechanical property and biodegradation improvement of wollastonite bioceramic through magnesium dilute doping. *J Mech Behav Biomed Mater*, 54:60-71.
https://doi.org/10.1016/j.jmbbm.2015.09.012

Xu Q, Chang ML, Zhang Y, et al., 2020. PDA/CU bioactive hydrogel with “hot ions effect” for inhibition of drug-resistant bacteria and enhancement of infectious skin wound healing. *ACS Appl Mater Interfaces*, 12(28):31255-31269.
https://doi.org/10.1021/acsami.0c08890

Yang YW, Cheng Y, Deng F, et al., 2021. A bifunctional bone scaffold combines osteogenesis and antibacterial activity via in situ grown hydroxyapatite and silver nanoparticles. *Bio-Des Manuf*, 4(3):452-468.
https://doi.org/10.1007/s42242-021-00130-x

Yang ZF, Feng FF, Jiang WW, et al., 2022. Designment of polydopamine/bacterial cellulose incorporating copper (II) sulfate as an antibacterial wound dressing. *Biomater Adv*, 134:112591.
https://doi.org/10.1016/j.msec.2021.112591

Ye J, Yao QQ, Mo AC, et al., 2011. Effects of an antibacterial membrane on osteoblast-like cells in vitro. *Int J Nanomedicine*, 6:1853-1861.
https://doi.org/10.2147/ijn.S17749

Zhang C, Ou Y, Lei WX, et al., 2016. $CuSO_4/H_2O_2$-induced rapid deposition of polydopamine coatings with high uniformity and enhanced stability. *Angew Chem Int Ed*, 55(9): 3054-3057.
https://doi.org/10.1002/anie.201510724

Zhao MH, Chen XP, Wang Q, 2014. Wetting failure of hydrophilic surfaces promoted by surface roughness. *Sci Rep*, 4:5376.
https://doi.org/10.1038/srep05376

Zhou L, Li X, Wang KB, et al., 2020. Cu^{II}-loaded polydopamine coatings with *in situ* nitric oxide generation function for improved hemocompatibility. *Regen Biomater*, 7(2): 153-160.
https://doi.org/10.1093/rb/rbz043

Zhu ZQ, Gao Q, Long ZY, et al., 2021. Polydopamine/poly (sulfobetaine methacrylate) Co-deposition coatings triggered by $CuSO_4/H_2O_2$ on implants for improved surface hemocompatibility and antibacterial activity. *Bioact Mater*, 6(8):2546-2556.
https://doi.org/10.1016/j.bioactmat.2021.01.025

Supplementary information

Tables S1 and S2; Figs. S1 and S2